Computer and laboratory studies on the aerodynamics of the NACA 65(1)-412 at Reynolds number 20 000

Joseph D. Tank,[1]
University of Southern California, Los Angeles, California, 90089-1191, United States

Bjoern F. Klose,[2] Gustaaf B. Jacobs[3]
San Diego State University, San Diego, California, 92182-1308, United States

Geoffrey R. Spedding[4]
University of Southern California, Los Angeles, California, 90089-1191, United States

When chord-based Reynolds numbers (Re) lie in the range $10^4 - 10^5$, even global and time-averaged quantities can be difficult to measure, predict and control. It is now possible to run direct numerical simulations and detailed experiments at the same Re, to reveal a rich and varying range of flow phenomena with sensitive dependence on boundary conditions and possible environmental disturbances. Here we make a close comparison for one geometry over a range of angles of attack, demonstrating abrupt changes in flow states and complex flows in the different regimes. These regimes and transitions will have practical consequences in any subsequent control strategy and exploration.

Nomenclature

AR	=	aspect ratio = b/c
b	=	span, m
c	=	chord, m
c_l, c_d	=	two-dimensional lift and drag coefficients
$c_{d,min}$	=	minimum drag value
$c_{l,\alpha}$	=	lift curve slope, 1/rad
f	=	frequency, Hz

---

[1] Graduate Student, Department of Aerospace and Mechanical Engineering
[2] Graduate Student, Department of Aerospace Engineering, AIAA Member
[3] Professor, Department of Aerospace Engineering, Associate Fellow
[4] Professor, Department of Aerospace and Mechanical Engineering, AIAA Member

L, D	=	lift and drag, N
Re	=	chord-based Reynolds number $= Uc/\nu$
t	=	time, s
St	=	Strouhal number $= fc/U$
T	=	turbulence intensity
U	=	mean flow speed, m/s
u, v, w	=	instantaneous velocity in $\{x. y. z\}$
$\bar{u}, \bar{v}, \bar{w}$	=	time-averaged velocity in $\{x. y. z\}$
x, y, z	=	coordinates in streamwise, spanwise, and normal directions
X,W,H	=	length, width, and height of test section
x_p	=	coordinate in direction parallel to airfoil chord
α	=	angle of attack, deg
α_crit	=	critical angle of attack, deg
α_0L	=	zero lift angle of attack, deg
δ_{lam}	=	laminar boundary layer thickness
δ_turb	=	turbulent boundary layer thickness
$\omega_x, \omega_y, \omega_z$	=	vorticity component in $\{x, y, z\}$

I.Introduction

AS practical small-scale flying devices proliferate and as interest in wind turbines and general turbomachinery of various scales develops, it becomes increasingly important to understand and characterize flows at moderate Reynolds number, where initial boundary layers are laminar, but where transition to turbulence somewhere over the foil or wing is possible. The likelihood and location of this transitional event governs large scale departures from linear behavior, and is accompanied by unusual sensitivity to small perturbations, in geometry or freestream conditions. The range of Reynolds numbers in question is approximately $10^4 < \mathrm{Re} < 10^5$, where $\mathrm{Re} = Uc/\nu$ (U is the flight speed, or mean freestream, c is a mean or local chord length, and ν is the kinematic viscosity). This regime is accessible to experiments in wind tunnels (though special care must be taken to resolve much smaller forces than customary) and also to direct numerical simulation (DNS) where discrete Navier-Stokes solutions can be computed on a fine mesh, with no modeling approximations.

In this Re range, the boundary layer always separates before the trailing edge, and, if transition to a turbulent state occurs quickly enough, can sometimes reattach to the airfoil surface in a time-averaged sense to form a laminar separation bubble (LSB). Unlike at the higher Re ($>10^6$), LSB formation generally improves aerodynamic performance (decrease c_d, increase c_l, increase L/D) at moderate Re, because a reattached flow reduces wake losses. Therefore, a flow controller that can force earlier boundary layer transition and LSB formation could greatly improve airfoil performance. The large amount of flow-field information generated from direct numerical simulations (DNS) can be used to develop and test data driven or physics based models for a flow controller, but previous studies have shown that computations may not agree with experiments even in standard test cases [1]. Here we use a mix of laboratory and numerical methods to detail the flow fields and forces on an airfoil at moderate Re, and determine means of comparison to test whether the different techniques expose the same physics.

II. Materials and Methods

A. Wind tunnel and models

PIV and force balance tests were run in the octagonal test section of the Dryden Wind Tunnel (DWT), (1.37 m span, $T < 0.035\%$ for disturbances between 10 Hz $< f <$ 1000 Hz). All models were milled from aluminum using a CNC mill with a precision of 0.0127 mm. The models used in the PIV tests had $c = 0.075$ m and $b = 0.225$ m, for $AR = 3$. Force balance tests were carried out using the $AR = 3$ model as well as an $AR = 12.9$ model ($c = 0.055$ m, $b = 0.71$ m). The larger AR (and area) model was used to generate forces that could be measured most accurately with the DWT force balance at Re $= 2\times10^4$. Time-averaged lift and drag curves generated with both models could be compared at Re $= 4\times10^4$, where both models generated forces in an appropriate range for the balance. Because of the relative sizes of the test section and the models, blockage effects were negligible. Two endplates sandwiched the wing to eliminate wing tip vortices and approximate a two-dimensional geometry.

B. Particle image velocimetry

During PIV tests, the tunnel was filled with glycerin-based smoke and a laser sheet parallel to the flow direction (in $\{x, z\}$) was generated by a double-pulsed Nd:YAG laser. A digital camera (1600 × 1200 pixel, 14 bit) imaged particle fields on a cross-section at mid-span ($y = 0$). Two wing models that were mirror images of each other were used to collect data over both the pressure and suction surfaces of the airfoil. α was set by alignment with a row on the digital image array, with an estimated uncertainty of $0.2°$.

In order to increase spatial resolution, the flow field was split into either five (for $\alpha = [0º, 2º, 4º, 6º, 8º, 10º]$) or two (for $\alpha = [10º, 10.1º, 10.2º, 10.3º, 10.4º, 10.5º]$) overlapping sub-regions. When two sub-regions are used, they correspond to the forward and the aft sections of the suction side of the airfoil. When five sub-regions are used, they correspond to the forward and aft sections of both the suction and the pressure sides of the airfoil, and the wake. 1000 image pairs were captured for each sub-region at a sampling rate of 9.6 Hz. This sampling rate was not sufficient to provide time-resolved data, but did allow for the generation and analysis of time-averaged and instantaneous flow fields. The images were processed with LaVision's DaVis software to produce velocity field estimates (u,w) on a uniform grid using a multi-pass algorithm, which had interrogation windows that were reduced to either 16×16, 8×8, or 6×6 pixels for the final pass. A 50% interrogation box overlap gave a final spatial resolution of [3, 4, 8] pixels, which is [0.11, 0.14, 0.28] mm. This is [0.08, 0.11, 0.21]× δ_{lam} or [0.06, 0.07, 0.15]× δ_{turb}, where $\delta_{lam} = \frac{5x}{\sqrt{Re}}$ and $\delta_{turb} = \frac{0.37x}{Re^{1/5}}$ are the laminar and turbulent boundary layer thickness at $0.5c$ of a flat plate with the same chord length as the model used.

All 1000 instantaneous velocity fields were averaged to produce one, time-averaged velocity field, $(\bar{u}, \bar{w})$, for each sub-region. The Matlab thin-plate smoothing spline function ("tpaps") has a single smoothing parameter that is similar to the smoothing parameter in Ref. [2], and was used to interpolate missing data, remove random noise contamination, and impose a certain smoothness constraint that is physically-reasonable for a viscous fluid flow. The time-averaged spanwise component of vorticity, $\bar{\omega}_y = \frac{\partial \bar{w}}{\partial x} - \frac{\partial \bar{u}}{\partial z}$, was calculated at each grid location from the derivatives of the smoothing spline coefficients. The sub-region velocity/vorticity fields were finally combined to form one composite velocity/vorticity field for each α.

C. Force measurements

Force measurements were performed with a custom, three-component force balance, which measures forces normal and tangent to the chord of the wing. These forces were converted to lift and drag, defined with respect to the freestream, as conventional. A new calibration, with forces chosen to span those that would be seen in the test, was performed before each test, generating a 3x4 calibration matrix which converts voltage outputs to force units. The three most recent calibration matrices were averaged to generate the final calibration matrix used during the test. Based on calibrations and measurements at typical loading conditions, the measurement uncertainty is less than 5 mN for

forces tangent to the chord of the wing. The measurement uncertainty for forces normal to the chord of the wing are less than 15 mN for the same force range. Both are small percentages of the true load (<10%).

Each time-averaged force balance test consisted of five sweeps, forward and backwards, through the entire α – range in increments of 0.5°. After each α - step, the flow was allowed to settle for ten seconds before ten seconds of data were collected at 5 kHz and averaged. The five sweeps produced ten time-averaged measurements for each α, which were averaged to obtain a single time-averaged value. This collection is reasonable if there is no hysteresis so that forward and backwards α-traverses give indistinguishable values. The uncertainty of each combined time-averaged force value was taken as the larger of either the standard deviation of the ten time-averaged measurements or the estimate of the force balance uncertainties given above. The entire test procedure was repeated at least three times to test for day to day repeatability.

D. Water channel flow visualization

Dye-injection flow visualization tests were carried out on a scaled model in the USC water channel (BWC) which has a rectangular test section (L,W,H = 762, 89, 61 cm). Free stream velocity data were collected during tests with a MSE 2D miniLDV laser Doppler velocimeter, and $T < 1.7\%$ for all tests. The airfoil model was made of clear acrylic with $c = 14.4$ cm, $b = 45$ cm ($AR = 3.1$). This AR is sufficient to generate a largely two dimensional flow at the mid-span location when tip vortices are blocked by the bottom of the channel at one end and an endplate positioned just beneath the free surface. Dye was injected from a leading edge exit port at $y/b = 0$ and/or at various offset (in $\{x, z\}$) locations upstream. Dye materials were milk and alcohol (mixed for neutral buoyancy) or fluorescein/rhodamine complexes. A 5.14 W, 532 nm wavelength CNI continuous wave laser was spread into a sheet in an (x, z)-plane and aligned in the y-direction with the injection location to illuminate the dye. A Mako U-130 camera (1280 × 1024 pixel, 10 bit) with an Edmund Optics 25 mm C series fixed focal length lens collected images at a frame rate of 20 fps from below the model through a window in the bottom of the channel. For Re = 2 x 10^4, $U = 14$ cm/s, and a convection time c/U is on the order of 1 s, so sampling 2 orders of magnitude faster can be considered time-resolved for this flow. The second advantage of dye visualization is that fine scale features can be observed and traced that are lost in an average PIV correlation box.

E. Vortex shedding frequency

Flow visualization images of the airfoil wake ($1 < x/c < 2$), captured in the BWC, were analyzed using a Matlab script to estimate the wake vortex shedding frequency as a function of α. Dye injected into the boundary layer marks these structures, and so the images were analyzed to determine how often patches of dye passed through the wake. This was done by selecting a grid of pixels (20 pixel × 20 pixel) from an interrogation box in the wake images and determining their intensity as a function of time. A spike in the intensity would indicate that a patch of dye (i.e. vortex structure) passed over the pixel. A Fourier transform was then used to generate an amplitude spectrum for each pixel, and the spectra from all pixels on the grid were averaged to determine the dominant frequencies in the wake. This method generally produced sharp, distinct peaks at low α, where vortices could be clearly identified, but less distinct peaks at the higher α, where the wake became more turbulent, leading to the diffusion of the dye streaks. When there was no obvious dominant frequency for a particular image set, or when the dominant frequency would change with the location of the interrogation box, that image set was discarded.

F. Numerical simulations

Numerical solutions of the flow field are obtained from compressible two and three-dimensional direct numerical simulation (DNS) using a nodal Discontinuous-Galerkin Spectral-Element Method (DGSEM) with explicit time integration.

In general notation, the Navier-Stokes equations can be written as a conservation law

$$Q_t = \nabla \cdot F$$

of the conserved variables

$$Q = [\rho \quad \rho u \quad \rho v \quad \rho w \quad \rho E]^T$$

where ρ, u, v, w, and E are the density, velocity components and inner energy respectively and F is the flux tensor:

$$\nabla \cdot F = F_x^a + G_y^a + H_z^a + Re^{-1}\left(F_x^v + G_y^v + H_z^v\right)$$

The indices a and v refer to the advective and viscous fluxes. They are defined as

$$F^a = [\rho u \quad p + \rho u^2 \quad \rho uv \quad \rho uw \quad u(\rho E + p)]^T$$

$$G^a = [\rho v \quad \rho vu \quad p + \rho v^2 \quad \rho vw \quad v(\rho E + p)]^T$$

$$H^a = [\rho w \quad \rho wu \quad \rho wv \quad p + \rho w^2 \quad w(\rho E + p)]^T$$

$$F^v = \left[0 \quad \tau_{xx} \quad \tau_{yx} \quad \tau_{zx} \quad \left(u\tau_{xx} + v\tau_{yx} + w\tau_{zx}\frac{\kappa}{(\gamma - 1)PrM_f^2}T_x\right)\right]^T$$

$$\boldsymbol{G}^v = \begin{bmatrix} 0 & \tau_{xy} & \tau_{yy} & \tau_{zy} & \left(u\tau_{xy} + v\tau_{yy} + w\tau_{zy} \dfrac{\kappa}{(\gamma-1)PrM_f^2} T_y \right) \end{bmatrix}^T$$

$$\boldsymbol{H}^v = \begin{bmatrix} 0 & \tau_{xz} & \tau_{yz} & \tau_{zz} & \left(u\tau_{xz} + v\tau_{yz} + w\tau_{zz} \dfrac{\kappa}{(\gamma-1)PrM_f^2} T_z \right) \end{bmatrix}^T$$

The system of equations is closed with the equation of state $p = \rho T / \gamma M^2$.

The solution vector is spatially approximated by a nth order polynomial within each spectral element and the fluxes are computed using a DG discretization scheme. The system of equations is integrated in time with a low-dispersion 4th-order explicit Runge-Kutta scheme. For a more detailed description of the method, we refer to Nelson *et al.* [3] and Kopriva [4].

The flow over a NACA 65(1)-412 airfoil is simulated at a Reynolds number based on the chord length of $Re_c =$ 20,000 and a Mach number of M = 0.3. The Mach number is relatively low ensuring a nominally incompressible flow, but it is high enough to prevent stability issues pertaining to the explicit time integration we use. We conduct a series of computations for different angles of attack from 0° to 10°.
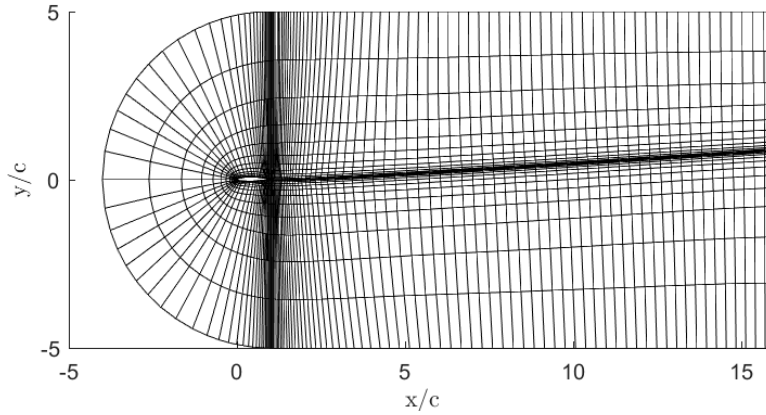
Fig. 1 Computational Domain with spectral elements.

For 2D simulations, the computational domain is given in Fig. 1 and consists of 2,256 quadrilateral elements, with the dimensions of the domain being adopted from Jones *et al.* [5]. The boundary elements are curved and fitted to a spline representing the airfoil's surface as described by Nelson *et al.* [3]. The outer boundaries of the domain are defined as free-stream boundaries while the airfoil surface is treated as a non-slip, adiabatic wall. In accordance with Nelson *et al.* [3], we use a twelfth order polynomial, which has been shown to give a converged solution. A kinetic energy conserving split-form approximation of the numerical fluxes, as described by Gassner *et al.* [6], is used to

ensure numerical stability of the scheme. The flow field and lift, drag, pressure, and skin friction coefficients and are averaged over ten convective time units.

For 3D simulations, the grid is adopted from Nelson [7], where the computational domain is extruded by half a chord length in spanwise direction and periodic boundary conditions are applied. This accounts to a total of 14,960 hexahedral spectral elements in the three-dimensional domain. For an angle of attack of 4°, a polynomial order of N = 12 is used. For higher angles of attack (8° and 10°), an h-refined mesh together with a sixth order polynomial ensures numerical stability. All three-dimensional simulations are initialized with results from two-dimensional computations.

Klose *et al.* [*] have discussed the 2D and 3D DNS results of the NACA 65(1)-412 airfoil in greater detail separately and show the existence of three different flow states at a Reynolds number of 20,000 within an angle of attack range of 3°.

[*] Bjoern F. Klose, Gustaaf B. Jacobs, Joseph Tank and Geoffrey R. Spedding: *Low Reynolds number airfoil aerodynamics: three different flow patterns within an angle of attack range of four degrees*, 2018 Fluid Dynamics Conference Atlanta, Georgia, 2018.

G. Laboratory and numerical experiment

One purpose of this study is to closely compare equivalent investigative procedures. Numerical simulations solve the known Navier-Stokes equations, albeit on a discrete grid. No modelling is used, but certain procedures may be required to regularize the solutions, particularly for low Mach number. The flow is fully resolved in space and time, with all velocity and pressure fields. The sensitivities of these transitional Re flows mean that high spatial resolution is required over large parts of the near-foil field, and calculations are expensive. Furthermore, each different U, or α, entails a completely new calculation because either Re or the problem geometry are now new. By contrast, wind tunnel or water channels have analog Navier-Stokes solutions, but to problems whose specifications are not precisely known. If these can be made sufficiently close to the nominal (ideal) problem geometry, then systematic variations in U and α can reveal dependencies in an efficient way.

Finally, experiments must be interrogated with specific measurement techniques, each of which yield estimates of selected quantities in some reduced dimension of the full physical field. Here Re = 2×10^4 is reachable by DNS with no model. The flow quality in the wind tunnel is good down to a certain minimum, which sets a maximum on chord length. The strain gauge load cells have a lower noise floor which is fixed in mN, so the wing area must be sized

carefully for force measurement resolution. All force measurements require a certain strain and model support deflection, but this cannot be large compared with effective disturbance scales in the flow. As will be shown later, the optimal wing area and aspect ratio differ for force and flow field measurements, respectively, driving the design alternately to high and low aspect ratio wings. In a true infinite wing problem, or in a computational box with wrap-around end conditions, *AR* by design is not an important parameter. However, in a physical model, wall or end-plate boundary layers interact with the wing tips. The ways in which they do so will differ according to the wall/plate boundary conditions in wind tunnel or water channel experiments. The experiments described here thus cover a range of *AR* and Re to specifically illustrate their influence, and we make a deliberate mix of DNS (DG), wind tunnel (WT) and water channel (WC) experiments, deducing most likely physical truths from overlap.

III. Results

A. Time-averaged lift and drag

The time-averaged c_l and c_d as well as the inviscid thin airfoil theory prediction (assuming the experimental α_{0L}) are given over a range of α in Fig. 2. The lift-slope $\left(\frac{\partial c_l}{\partial \alpha} \equiv c_{l,\alpha}\right)$ is close to 2π, for small α. Note how $\alpha_{0L} > 0$ ($c_l < 0$ at $\alpha = 0^\circ$), even when the camber is positive, suggesting an effective negative camber at low α due to flow separation. This behavior is significantly different than at a design Re = 10^6, where $\alpha_{0L} < 0$ and design $\alpha \approx 0$ [8].

At $\alpha = 4^\circ$, DNS and WT c_l agree and lie below the inviscid prediction. At $\alpha = 8^\circ$, DNS and WT c_l do not agree: DNS is above the 2π line, a state not reached in experiment until $\alpha = 9.5^\circ$. At $\alpha = 10^\circ$, DNS and WT c_l agree once more, and both exceed the inviscid value.

WT $c_l < 0$ when $c_{d,min}$ is reached at approximately $\alpha = -1.5^\circ$. As α decreases below -1.5°, c_l no longer falls with slope 2π, departing, once again, abruptly, from the inviscid line. Disagreements in c_d occur at the same α as those in c_l. Both show an abrupt improvement in performance (decrease in c_d, increase in c_l) at some critical angle of attack (α_{crit}).

The lift-drag polar shows the abrupt jump in experimentally measured forces at a critical angle of attack, α_{crit}. It will be shown later that the jump to the high-lift low-drag state is due to the formation of a laminar separation bubble (LSB). As noted before, in this Re range, the increase in *L/D* due to bubble formation is opposite to what is often reported at Re > 10^5.
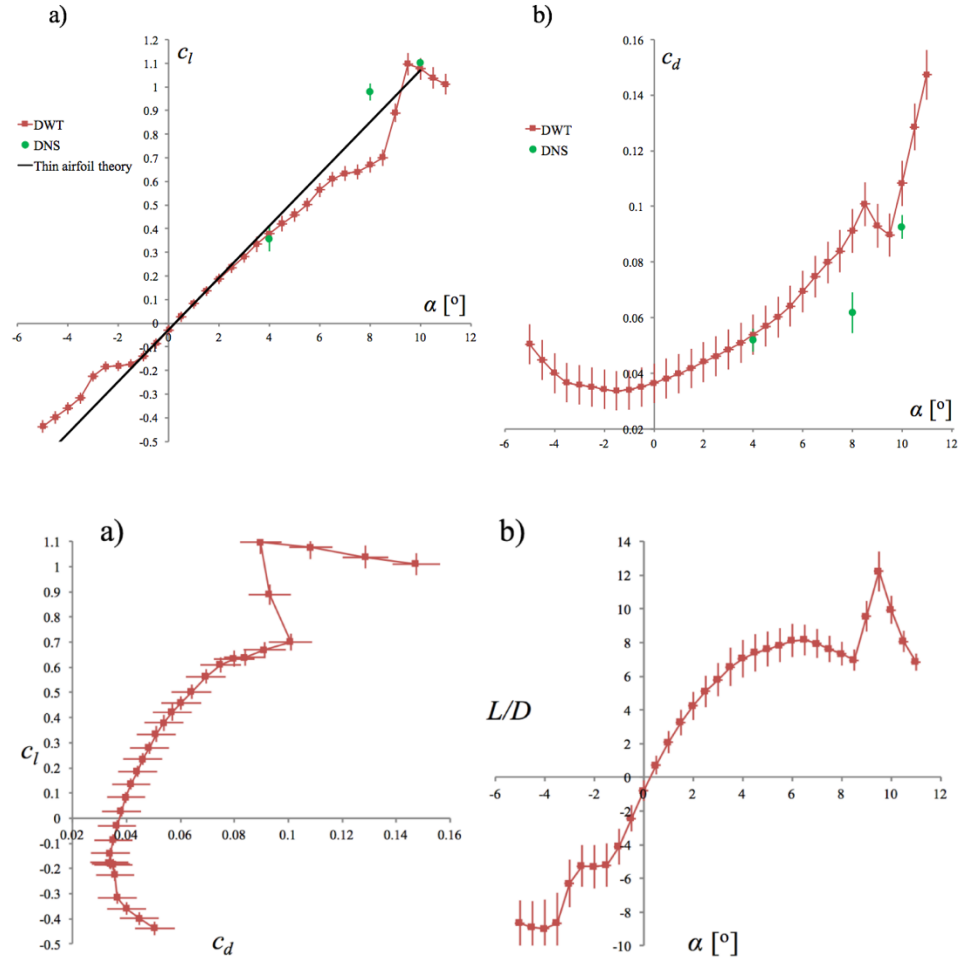
Fig. 2 Time-averaged $c_l(\alpha)$, $c_d(\alpha)$ in (a) and (b), and the polar $c_d(c_l)$ and $L/D(\alpha)$ in (c), (d) for the NACA 65(1)-412 at Re = 2 × 10^4.

The disagreement between WT and DNS comes from different α_{crit}. α_{crit} is hard to estimate with great accuracy in experiments, as any real experiment is influenced by the free stream disturbance environment, model and tunnel vibrations, surface roughness, and model *AR*, to name a few. The sensitivity to *AR* has been investigated, and Fig. 3 gives c_l and c_d for two wings, *AR* = 3 and 13, sized for Re = 4 x 10^4 and tested under identical conditions. Recall that α_{crit} = 9.5° for WT at Re = 2 x 10^4. In Fig. 3, α_{crit} =8° for *AR* = 3 and α_{crit} = 7° or 7.5° (depending on sweep direction) for *AR* = 13, and therefore α_{crit} is clearly a function of both Re and *AR*.
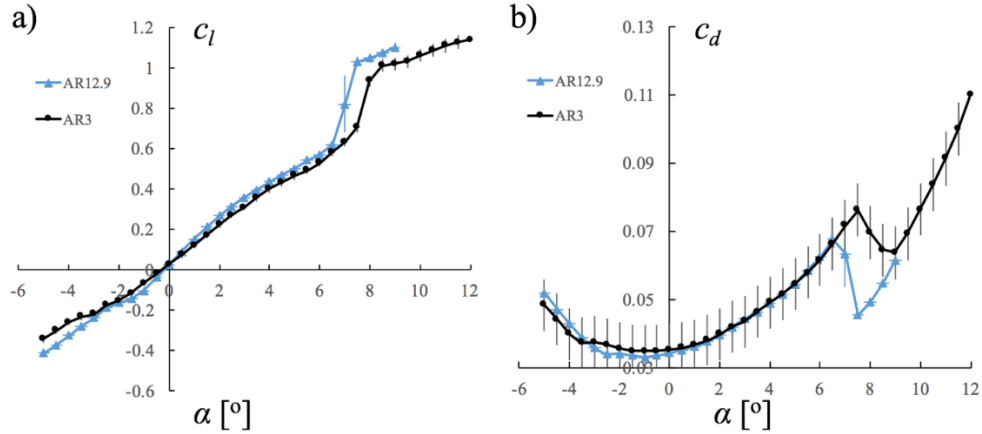
Fig. 3 $c_l(\alpha)$, $c_d(\alpha)$ in (a) and (b), at Re = 4×10^4 for $AR = 3$ and $AR = 13$

The relative importance of end effects, which appear to increase α_{crit}, diminish with increasing AR, so α_{crit} in any experiment will likely be lower than the corresponding DNS value, as is seen in Fig. 2. This also means that PIV data derived from the $AR = 3$ wing will show a different α_{crit} than the force balance data derived from an $AR = 13$ wing in the same facility, as evidenced by the curves in Fig. 3. However, if we disregard the particular value of α_{crit}, then the flow physics near mid span and the transition from a fully separated state (SI) to a reattached state (SII) will be the same, so dynamically equivalent flow fields can now be compared around that transition.

B. Flow topology – time-averaged fields

The jump from SI to SII seen in the c_l and c_d plots of Fig. 2 is caused by the separated boundary layer reattaching to the airfoil surface at α_{crit} [9]. The development of the time-averaged flow before α_{crit} is shown in Fig. 4 using PIV-generated streamlines. At $\alpha = 0°$, the flow separates before the trailing edge over the suction (upper) surface. A recirculating region (v1) extends over the airfoil and aft of the trailing edge. A counter-rotating vortex (v2) appears first to originate at the trailing edge from flow around the pressure (lower) side. As v1 grows with increasing α, v2 is increasingly distorted and displaced downstream, appearing more as a secondary structure that is induced by v1. A comparison of streamlines from DNS and experiment for $\alpha = 0°$ is shown in Fig. 5. At $\alpha = 10°$, a blue line has been added that encloses the airfoil as well as the viscous recirculating regions. The recirculating fluid has about the same cross-section as the airfoil itself, and a similar vertical displacement. It could be described as a large LSB with virtual reattachment in the wake, aft of the physical trailing edge. The global flow field and streamline deflection (and hence the lift) is determined by the effective airfoil shape, made up of the combined airfoil and LSB geometry.
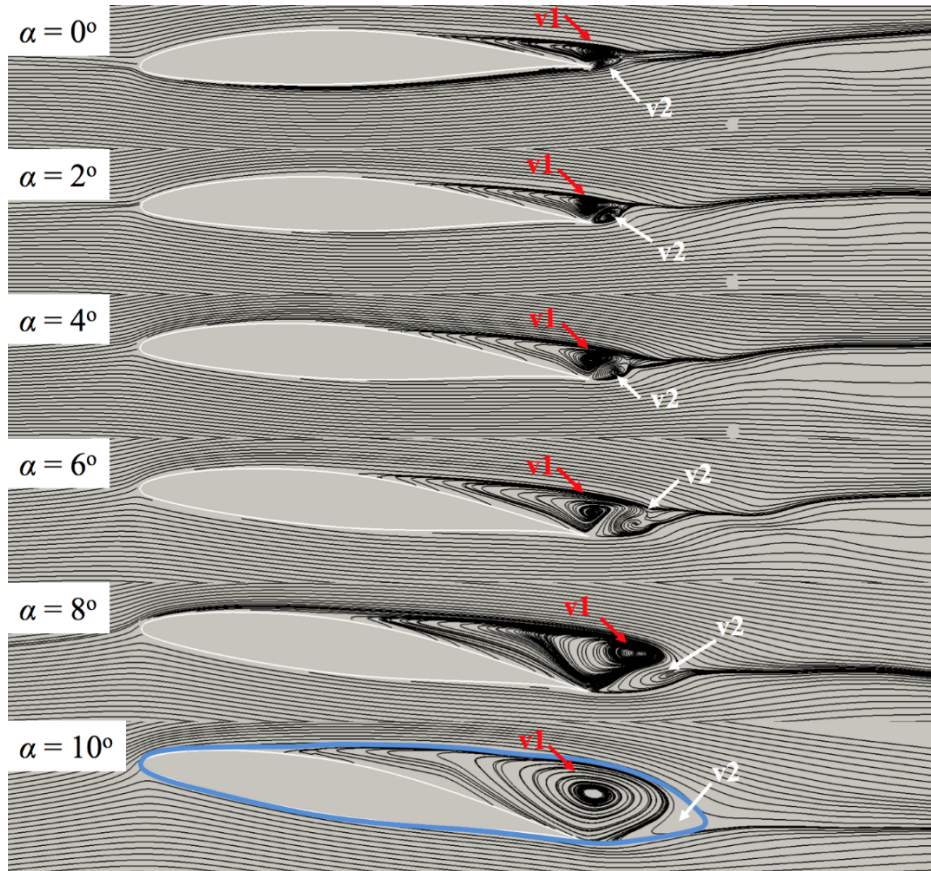
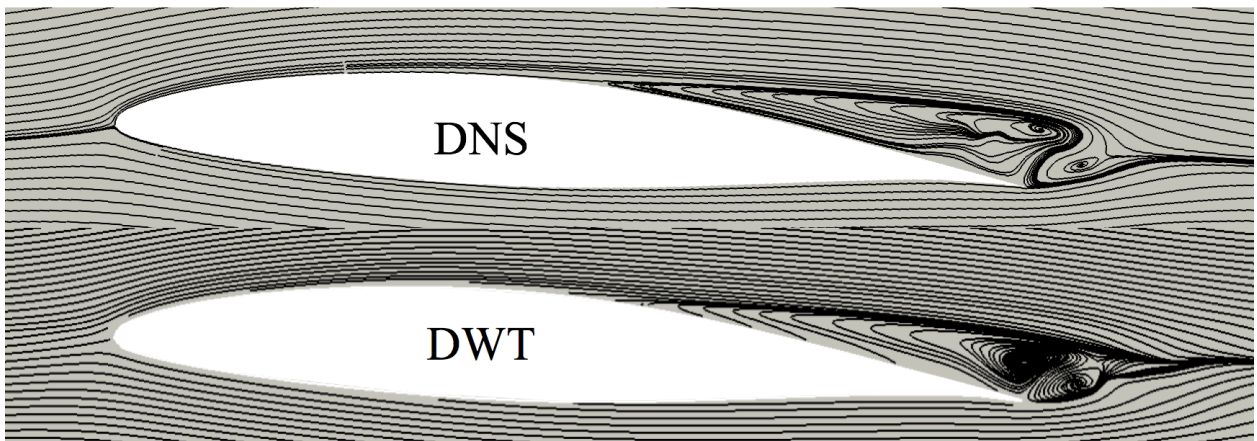**Fig. 4: Time-averaged streamlines for $\alpha < \alpha_{\text{crit}}$**

Fig. 5: Comparison of time-averaged streamlines from DNS and experiment for $\alpha = 4^{\text{o}}$

The laminar boundary layer appears to separate from the surface at a well-defined angle in Fig. 4, and Fig. 6 shows a systematic estimation of the shear layer position in chordwise and chord-normal coordinates.
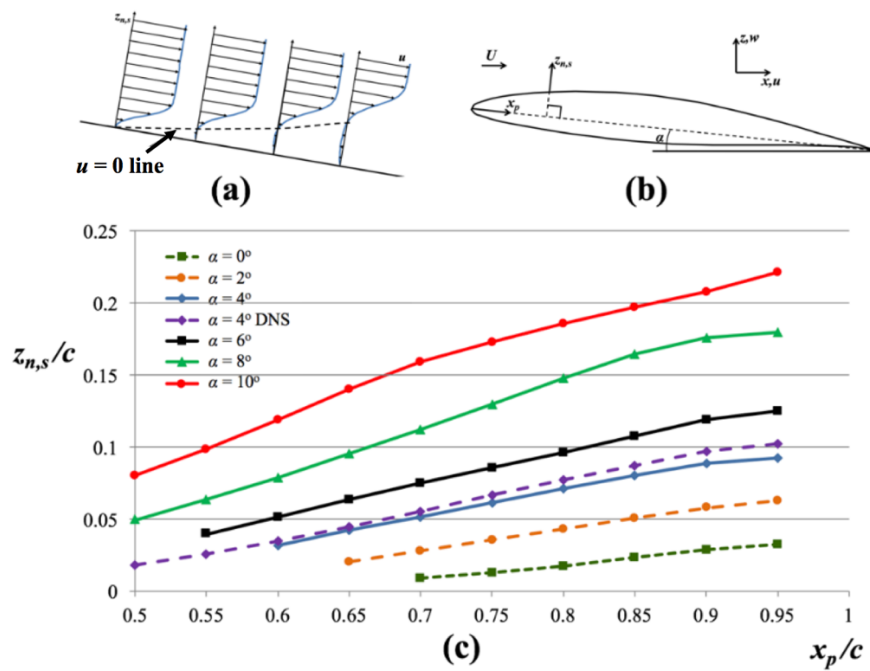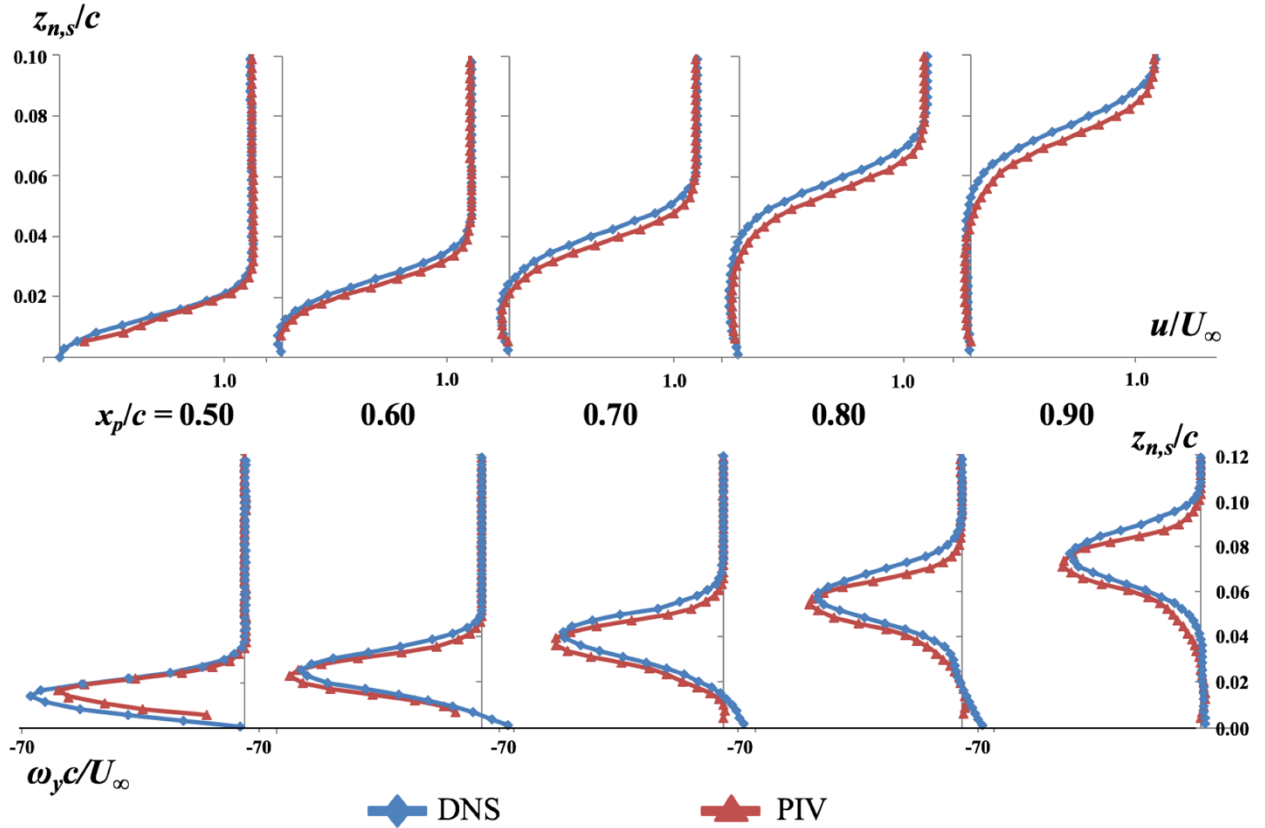
Fig. 6 a) $u = 0$ **line definition, b) coordinate system definition, c)** $u = 0$ **line locations from PIV for** $\alpha = [0^o - 10^o]$ **and DNS** $u = 0$ **line location for** $\alpha = 4^o$

More detailed comparisons of u- and ω_y- profiles at $\alpha = 4^o$ (Fig. 7) show reasonable qualitative agreement, though in DNS, the boundary layer diffuses away from the surface more rapidly with streamwise distance.

Fig. 7 *u*-profile (top) and $\bar{\omega}_y$-profile (bottom) comparison between DNS and PIV over the suction surface of the airfoil for $\alpha = 4^o$

At $\alpha = 10.0^o$ the slow recirculating region reaches it largest size (Fig. 4). The effective airfoil shape is not aerodynamically efficient, leading to a decrease in L/D after a local maximum but before α_{crit} (Fig. 2). At $\alpha = 10.1^o$, the flow state abruptly changes (Fig. 8). A laminar separation bubble forms and closes from about $1/3 - 2/3c$. With small further increases in α, the bubble moves forward and shortens. The formation of the LSB (transition from SI to SII) greatly increases L/D.
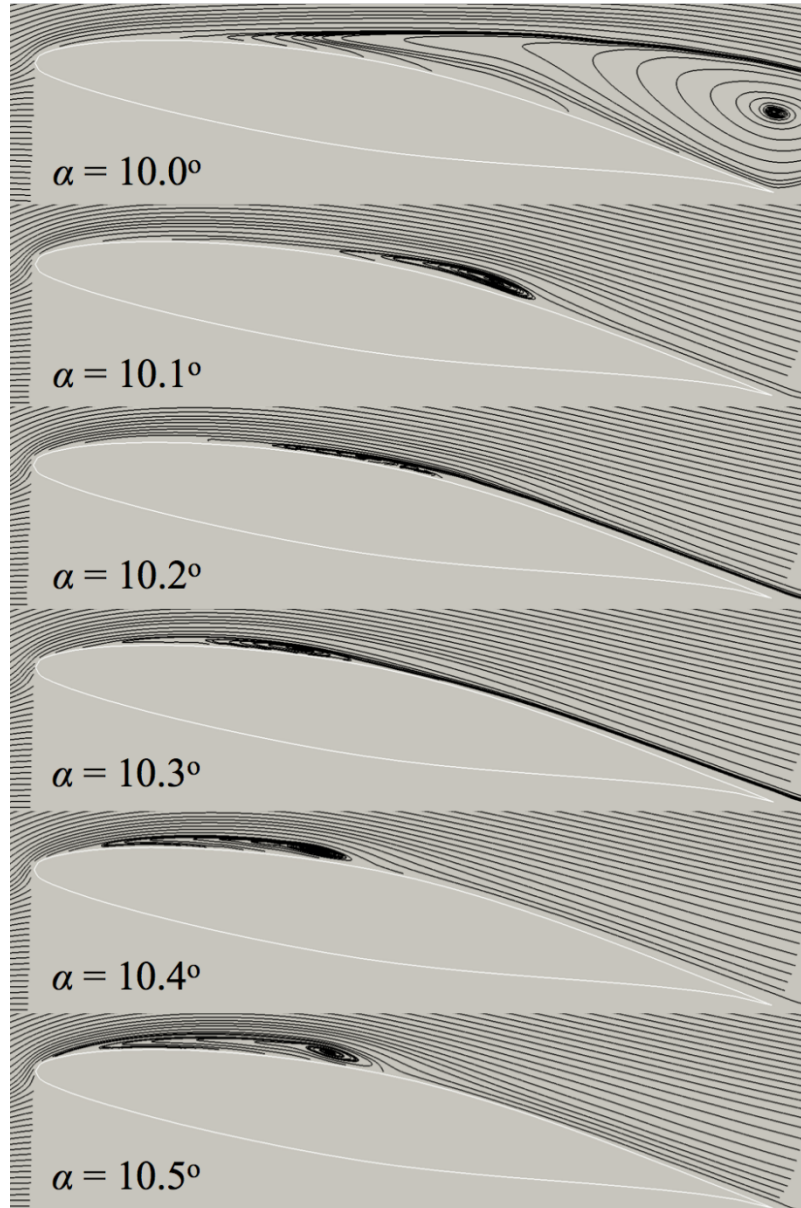
Fig. 8 Time-averaged streamlines close to α_{crit}.

C. Instantaneous flow fields

Three qualitatively distinct types of flow field can be identified from instantaneous PIV and dye injection images: type 1) laminar separation with vortex rollup beginning after the trailing edge; type 2) laminar separation with vortex rollup beginning over the airfoil and no reattachment; type 3) laminar separation with reattachment. Flow fields of type 1 and 2 occur before α_{crit} and type 3 occurs after α_{crit}. Examples of time-averaged and instantaneous flow fields of type 1, 2, and 3 can be found in the top, middle, and bottom row respectively of Fig. 9. PIV and dye injection

images of the same flow type look very similar, and the separation locations and angles at a given α are nearly identical. The main difference is that the dye injection images show a transition from flow field type 1 to type 2 and from flow field type 2 to type 3 at earlier α. This may be due in part to the much larger turbulence intensity in the water channel. When vortex rollup occurs after the trailing edge (type 1), the primary instability mode is a wake mode where two opposite-signed shear layers interact. With increasing α, the roll-up moves forward until it now occurs over the solid surface (type 2) and the primary instability mode is in the separated shear layer. Following transition to type 3, at and after α_{crit}, the first wavy motions can be seen in the shear layer of the short laminar separation bubble. It is the rapid growth of this mode that leads to pairing and transition and a flow that is reattached, in the mean, though no instantaneous flow field resembles this mean.
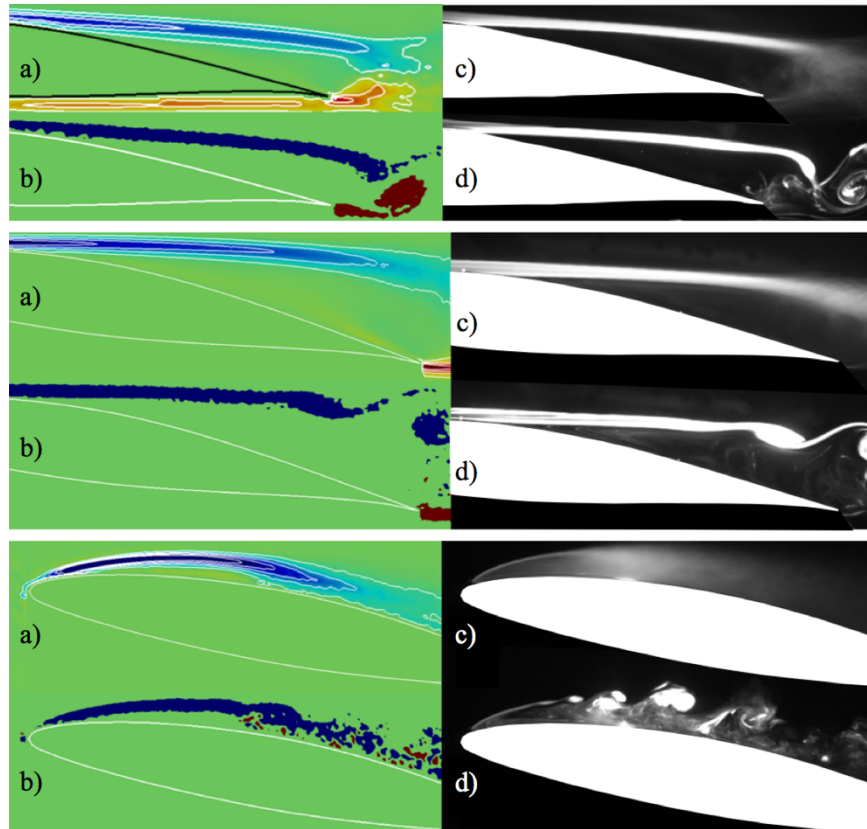

Fig. 9: a) time-averaged ω_y from PIV, b) instantaneous ω_y from PIV, c) time-averaged and d) instantaneous dye flow visualization images for $\alpha_{PIV} = \alpha_{DFV} = 4°$ (top), $\alpha_{PIV} = 9°$ $\alpha_{DFV} = 6°$ (middle), and $\alpha_{PIV} = \alpha_{DFV} = 11°$ (bottom).

D. Wake vortex shedding frequency

Wake vortex shedding frequency data from seven tests, expressed as the non-dimensional Strouhal number (St = fc/U), has been plotted for $\alpha < \alpha_{crit}$ (flow field types 1 and 2) in Fig. 10. Reliable measurements could not be made after α_{crit} because of the increased diffusion of dye before the trailing edge due to increased mixing in the reattached boundary layer when an LSB forms. St remains between 3 and 3.3 for $0^o < \alpha < 3.5^o$, but drops between $\alpha = 3.5^o – 4.5^o$ to approximately 2.6, before increasing to approximately 3.25 at $\alpha = 5^o$ and remaining nearly constant until $\alpha = 8^o$. Three data points for $6^o < \alpha < 7^o$ fall between 1.5 and 1.62, corresponding to approximately half the mean values for all other tests. The existence of prominent first subharmonics suggest a vortex pairing or merging process.
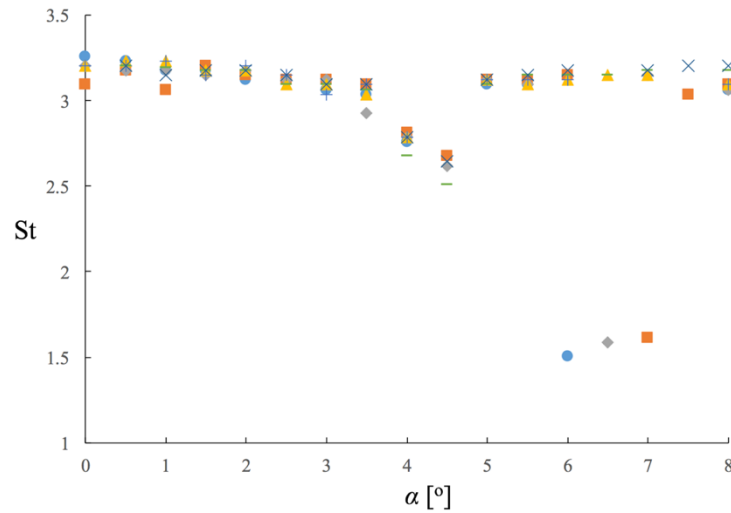
Fig. 10: St variation with α. Seven different tests are overlaid for nominally identical conditions for any given α.

St can be determined using DNS force time traces, as wake vortex shedding will cause oscillations in lift and drag. DNS St values at $\alpha = 0^o$ and 4° fall within the same range as experimental data. However, DNS gives St = 1.9 at $\alpha = 6^o$, which is below most experimental values. It is interesting to note that it appears this value would agree with experimental data had the experimental data continued to fall at the rate seen between $\alpha = 3.5^o – 4.5^o$. Fair comparisons cannot be made at higher α, as the experiment and DNS show the airfoil in different flow states.

The jump in St seen between $\alpha = 4.5^o$ and 5° may be associated with the switching of the dominant instability that leads to wake vortex shedding from a shear layer instability to a wake instability as the flow field switches from type 1 to type 2. The switching between type 1 and type 2 flow fields was found to occur at 5.5^o +/- 0.5^o. However, it should

be noted that an upstream disturbance can create a dye filament pattern that may persist into the wake. This means that some wake patterns, and therefore frequency measurements, may be impacted by disturbances that have since evolved or died out. It is also not known how large the wake vortex formation region is, and how measurements are impacted by their proximity to this region. Finally, dominant frequencies become harder to measure using the current method as the wake becomes more turbulent at the higher α. Further hotwire tests are suggested to investigate the wake vortex shedding frequency in more detail.

IV.Conclusion

a. The flow is very rich and complex with a number of qualitatively different regimes over varying α.

b. There are two flow regimes that have previously [9] been called SI (a low lift state where forces are determined by the location of the inevitable laminar separation before the trailing edge) and SII (where the laminar separation is followed by reattachment, in the eman sense, behind a laminar separation bubble). This second state, SII, has higher L/D than SI, and so may be viewed as a preferred state. Their co-existence seems quite robust over different experimental/numerical methods, though exact values of α_{crit} vary. The abrupt transition between SI and SII at α_{crit} is sensitive to small disturbances though by the same token offers potential for efficient control.

c. Between SI and SII the closed LSB moves forward on the wing section and simulations reveal a very regular, quasi-2D structure here, close to α_{crit}. It is this state, and disturbances to it that could hold the key to controlling the sensitivity.

c. Proper comparisons between experiment and numerical simulations need to take into account the physical constraints. Most experiments are contaminated to some extent by wall boundary conditions, model vibration and deflection, and by variations in the freestream, the latter commonly described by a single number. When the physical system is one that displays extreme sensitivity to small disturbances, as does this one (and by design) there are limits on how much agreement can be expected between different realizations (experiment – experiment, experiment – simulation, simulation – simulation). An informed interpretation is required to understand any realization, or pairwise comparison of them.

d. There is no reason to suppose that the phenomena here are exceptional or particular to this airfoil geometry. Rather, we expect and propose that the same basic flow types, and transitions between them, will be found in sufficiently careful experiment or simulation for many airfoils and wings at moderate Re.

References

[1] Tank, J., Smith, L., Spedding, G.R. "On the possibility (or lack thereof) of agreement between experiment and computation of flows over wings at moderate Reynolds number," *J R Soc Interface*. **7**, December 2017. DOI: 10.1098/rsfs.2016.0076

[2] Spedding G.R., Rignot, E.J. "Performance analysis and application of grid interpolation techniques for fluid flows," *Exp Fluids*, Vol. 16, Issue 6, 1993, pp. 417-430.

[3] Nelson, D. A., Jacobs, G. B., and Kopriva, D. A., "Effect of Boundary Representation on Viscous, Separated Flows in a Discontinuous-Galerkin Navier-Stokes Solver", Theoretical Computational Fluid Dynamics, Vol. 30, 2016, pp. 363-385.

[4] Kopriva, D. A., "Implementing Spectral Methods for Partial Differential Equations", Springer, New York, 2009.

[5] Jones, L. E., Sandberg, R. D., and Sandham, N. D., "Direct numerical simulations of forced and unforced separation bubbles on an airfoil at incidence", Journal of Fluid Mechanics, Vol. 602, 2008, pp. 175-207.

[6] Gassner, G. J., Winters, A. R., and Kopriva, D. A., "Split form nodal discontinuous Galerkin schemes with summation-by-parts property for the compressible Euler equations", Journal of Computational Physics, Vol. 327, 2016, pp. 39-66.

[7] Nelson, D. A. and Jacobs, G. B., "High-order visualization of three-dimensional lagrangian coherent structures with DG-FTLE", Computers and Fluids, Vol. 139, 2016, pp. 197-215.

[8] Abbot, I.H., von Doenhoff, A.E. *Theory of Wing Sections Including a Summary of Airfoil Data*. General Publishing Company, Toronto, 1959, pp. 622

[9] Yang, S.L., Spedding, G.R. "Separation Control by External Acoustic Excitation at Low Reynolds Numbers," *AIAA*, Vol. 51, No. 6, 2013, pp. 1506 – 1515. DOI: 10.2514/1.J051469